

GenMFSR: Generative Multi-Frame Image Restoration and Super-Resolution

Harshana Weligampola^{1,2}, Joshua Peter Ebenezer¹, Weidi Liu¹, Abhinav K. Venkataramanan¹,
Sreenithy Chandran¹, Seok-Jun Lee¹, and Hamid Rahim Sheikh¹
¹Samsung Research America, ²Purdue University

wweligam@purdue.edu

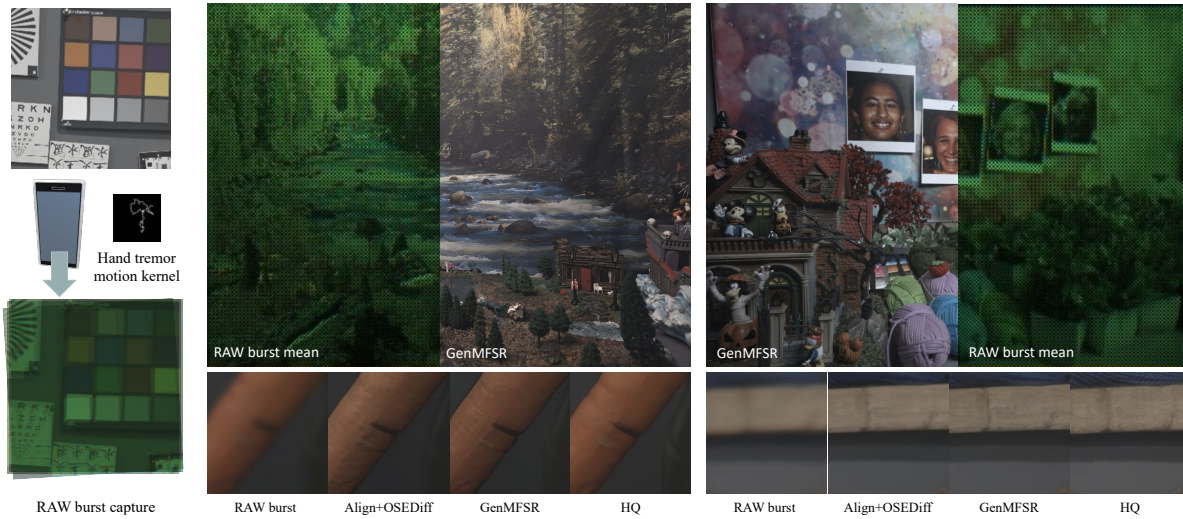


Figure 1. GenMFSR: Superior high-frequency feature generation from multi-frame RAW images via a unified denoising, demosaicing, registration, and super-resolution model in a single-step.

Abstract

Camera pipelines receive raw Bayer-format frames that need to be denoised, demosaiced, and often super-resolved. Multiple frames are captured to utilize natural hand tremors and enhance resolution. Multi-frame super-resolution is therefore a fundamental problem in camera pipelines. Existing adversarial methods are constrained by the quality of ground truth. We propose **GenMFSR**, the first Generative Multi-Frame Raw-to-RGB Super Resolution pipeline, that incorporates image priors from foundation models to obtain sub-pixel information for camera ISP applications. GenMFSR can align multiple raw frames, unlike existing single-frame super-resolution methods, and we propose a loss term that restricts generation to high-frequency regions in the raw domain, thus preventing low-frequency artifacts.

1. Introduction

Multi-frame super-resolution (MFSR) is the cornerstone of modern mobile computational photography, relying on natural hand tremors to recover sub-pixel details from noisy RAW bursts. Standard Image Signal Processors (ISPs) apply sequential, lossy modules (demosaicing, denoising) that destroy critical sensor-level information. While recent generative models (e.g., DarkDiff [45], RDDM [4], ISPDiffuser [25]) achieve unprecedented photorealism for single RAW images, integrating these priors into the temporally misaligned multi-frame RAW pipeline remains unsolved. Current multi-frame approaches [12, 37] rely on deterministic regression, which converges to posterior means and produces over-smoothed, “waxy” textures rather than photorealistic details.

Generative diffusion priors can synthesize these missing high-frequency details. However, applying them to the RAW-to-RGB inverse problem introduces a critical failure mode: *domain collision*. Standard priors are trained on

highly processed, non-linear sRGB images. When forced to regularize linear, mosaiced sensor data, prior attempts to aggressively “correct” the low-frequency structure (e.g., global color and macro-geometry) already recoverable from the burst result in severe structural hallucinations.

We develop a principled remedy for this collision. In burst reconstruction, low-frequency components are effectively determined by aligned sensor measurements, leaving only high-frequency textures underdetermined. Therefore, we treat the generative prior as an *orthogonal score projection* via a High-Frequency Variational Score Distillation (HF-VSD) loss. By applying a frequency-domain mask to the score gradients, we restrict the prior’s corrective power strictly to the unobserved high-frequency latent subspace, successfully preventing hallucinations while synthesizing photorealistic textures.

To translate this theory into a practical mobile pipeline, we propose GenMFSR, an end-to-end, single-shot generative restoration framework. We embed Spatial Transformer Networks (STNs) directly within the multi-frame encoder for native sensor-domain alignment, bypassing massive external registration networks. By leveraging low-rank adaptation (LoRA) and one-step distillation, GenMFSR maintains the expressive power of a frozen pretrained decoder while reducing latency to a single forward pass.

In summary, GenMFSR selectively leverages a strong generative prior while strictly preserving the deterministic information present in aligned raw measurements. Our main contributions are:

- **First Generative RAW MFSR Pipeline:** We demonstrate the first burst RAW to RGB diffusion model, which can handle unregistered RAW frames while leveraging the generative capabilities of foundation models.
- **Subspace-Projected Score Distillation (HF-VSD):** We introduce a new diffusion loss function called subspace-projected score distillation that reduces low frequency hallucinations in the raw domain.
- **Native Generative Alignment & Latent Bridging:** We introduce a new encoder that maps linear, unregistered, mosaic RAW data directly into the latent space of a pretrained diffusion model.
- **Empirical Handheld Motion Simulation:** We construct a rigorous paired burst dataset by extracting and applying real-world continuous hand-tremor trajectories to static RAW captures, ensuring physically accurate evaluation.

Extensive quantitative and qualitative experiments demonstrate that GenMFSR achieves state-of-the-art perceptual quality, outperforming existing deterministic and generative baselines by yielding highly realistic, hallucination-free textures.

2. Related Work

Burst Super-Resolution. Handheld burst photography relies on natural hand tremors to recover sub-pixel information [12, 37]. Recent learned methods, including Burstormer [10] and MFSR-GAN [16], achieve state-of-the-art alignment and fusion but rely heavily on deterministic regression or unstable adversarial objectives, fundamentally limiting their ability to synthesize absent high-frequency details.

By contrast, diffusion models offer a generative alternative with strong perceptual fidelity. While they have shown promise in single-frame super-resolution [8, 18, 32, 38], their application to multi-frame RAW-to-RGB burst captures remains underexplored.

Generative Priors in ISP. Latent diffusion models [27] have revolutionized single-image restoration [18, 38]. Recent industry frameworks (e.g., DarkDiff, RDDM, ISPDiffuser) successfully map single RAW captures to sRGB using diffusion priors. However, extending these priors to multi-frame bursts remains critically underexplored. Naively adapting single-frame models destroys temporal consistency, while standard distillation techniques like VSD [35] suffer from domain collisions when applied to RAW sensor data. Our work bridges this gap by introducing the first generative multi-frame RAW architecture with subspace-restricted distillation.

Model distillation: has been used as a knowledge transfer technique to create compact, efficient “student” models that mimic the behaviour of a larger, more complex “teacher” model. In the context of diffusion models [26], accelerated sampling and distillation have been used to drastically reduce the number of sampling steps from hundreds or thousands to just a few, enabling real-time generation [20, 21, 24, 30, 31, 38]. While earlier works [28] focused on finding “shortcuts” to progressively distill the teacher model, recent work by Wu *et al.* [38] used a regularization approach that is conceptually aligned with GANs, using an adversarial-style objective like Variational Score Distillation (VSD) [35] to enforce high-fidelity, plausible results.

Noise conditional generative models: Typical conditioning mechanisms, such as ControlNets [43], and Adapters [22], require training an additional, often large, encoding module. Beyond using noise as a simple prior, recent works [2, 6, 11, 33, 34] have explored using structured or conditional noise to guide the generative process. For instance, Dai *et al.* [6] demonstrated that conditioning on noise can control the generation process, though its efficacy can be limited by domain gaps between the input and output.

In this work, we propose a framework that integrates the efficiency of model distillation with explicit control over high-frequency generation. This allows our model to ef-

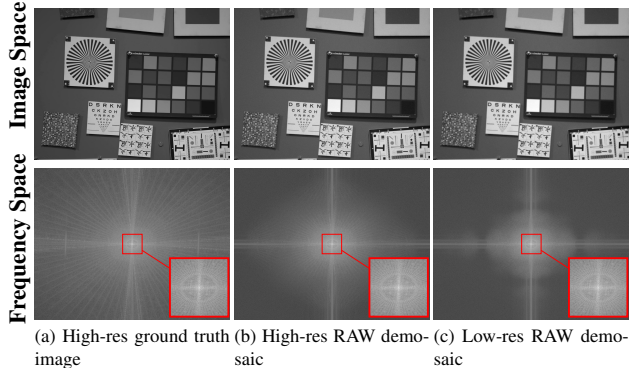


Figure 2. Comparison of RAW demosaiced images with the ground truth image in image and frequency space. Frequency-space figures are shown in the natural logarithm of the real frequency values.

fectively generate plausible high-frequency details, directly addressing a key limitation in deterministic reconstruction.

3. Motivational study

As shown in Fig. 2, we know that the problem of RAW-to-RGB super-resolution involves a significant frequency-domain gap. The low-resolution RAW input’s high-frequency regions are sparse and noisy. The generator’s task is to plausibly fill in this missing high-frequency information to match the ground truth. As highlighted, the low-frequency components remain largely unchanged in all domains. This leads to the idea of focusing on high-frequency feature generation without hindering low-frequency features. Generating low-frequency content can lead to hallucinations of objects which are undesirable for consumer camera applications.

4. Methodology

Our goal is to reconstruct a high-fidelity, photorealistic RGB image from a misaligned burst of RAW sensor data. In this section, we formalize the RAW-to-RGB pipeline as an inverse problem with partial observability. We then introduce our core theoretical contribution: a subspace-restricted prior integration technique (HF-VSD) that explicitly separates deterministic recovery from stochastic high-frequency synthesis. Finally, we detail the generative multi-frame architecture and optimization strategy used to solve this formulation.

4.1. Inverse Problem with Partial Observability

Given a burst of N RAW frames $\mathbf{y} = \{\mathbf{y}^{(i)}\}_{i=1}^N$, our objective is to reconstruct a high-resolution RGB image \mathbf{x} . Due to spatial downsampling, Poisson-Gaussian sensor noise, and Bayer mosaicing, the inverse mapping from \mathbf{y} to \mathbf{x} is highly ill-posed.

However, burst capture provides strong physical constraints on the scene. Because the burst acquisition operator, which is characterized by pixel aperture integration and sensor noise, attenuates high spatial frequencies much more severely than low frequencies, the inverse problem exhibits frequency-dependent determinacy. After temporal alignment and multi-frame fusion via sub-pixel shifts, the coarse geometry, global illumination, and structural color are largely determined by the measurements. In contrast, fine-scale textures remain underdetermined. We therefore conceptually decompose the target image into two approximately complementary subspaces under natural image statistics: $\mathbf{x} = \mathbf{x}_L + \mathbf{x}_H$, where \mathbf{x}_L represents the low-frequency components reliably inferred from the sensor data, and \mathbf{x}_H represents the high-frequency components that require prior-driven inference. This partial observability structure fundamentally motivates the selective integration of generative priors.

4.1.1. Training Objective and Optimization

The total training objective balances deterministic distortion and generative perception by anchoring the observable subspace and shaping the underdetermined subspace. We formulate this as a generation task regularized by a pre-trained diffusion prior:

$$\theta^* = \arg \min_{\theta} \mathbb{E}_{\mathbf{y}, \mathbf{x}} [\mathcal{L}_{\text{data}}(G_{\theta}(\mathbf{y}), \mathbf{x}) + \lambda \mathcal{L}_{\text{HF-VSD}}(G_{\theta}(\mathbf{y}))], \quad (1)$$

where \mathbf{x} is the ground-truth RGB image, λ is a balancing hyperparameter between $\mathcal{L}_{\text{data}}$ fidelity loss (comprising standard MSE and LPIPS losses calculated in the RGB pixel space), anchors the observable subspace, ensuring that the low-frequency structure and color perfectly match the ground truth, and $\mathcal{L}_{\text{HF-VSD}}$ regularization loss to regularize the generated images in a specified image prior which shapes the underdetermined subspace, guiding the latent representations to generate photorealistic textures without disrupting the data term’s structural consensus. We employ a one-step adversarial distillation strategy (combining LoRA fine-tuning with a discriminator) to make this robust regularization compatible with single-step inference.

4.2. Subspace-Restricted Prior Integration (HF-VSD)

Generative image priors [26], particularly latent diffusion models, offer a powerful mechanism for synthesizing the unobserved high-frequency detail \mathbf{x}_H . Standard score distillation techniques (e.g., VSD [35]) apply diffusion gradients over the full image distribution, effectively regularizing the reconstruction using the gradient of the log-likelihood: $\nabla_{\mathbf{x}} \log p(\mathbf{x})$. When applied to the RAW-to-RGB inverse problem, this global prior influences both \mathbf{x}_L and \mathbf{x}_H . However, because the diffusion model is trained

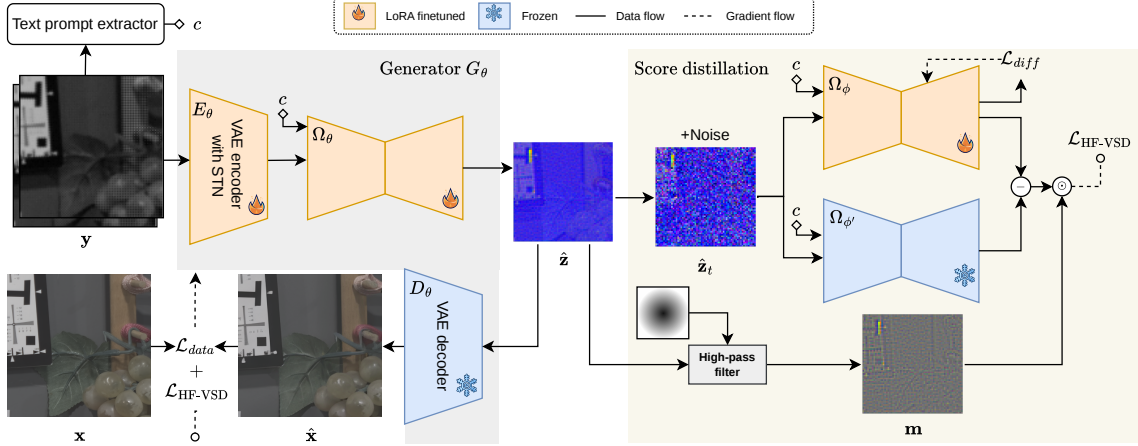


Figure 3. The end-to-end training framework for our proposed GenMFSR model. A multi-frame RAW encoder E_θ with embedded STN aligns and processes the input burst of raw images. A U-Net Ω_θ and frozen decoder D_θ generate the RGB image $\hat{\mathbf{x}}$. The framework is trained with a data fidelity loss \mathcal{L}_{data} and our regularization \mathcal{L}_{HF-VSD} , which uses a high-pass filter to ensure the diffusion prior focuses on high-frequency details.

exclusively on highly processed sRGB images, its low-frequency score estimates inherently conflict with the true low-frequency structure deterministically recovered from the RAW measurements. This ”domain collision” results in severe structural drift, color shifts, and low-frequency hallucinations (see Fig. 11).

To prevent prior-likelihood conflict, we treat score distillation as a projection operator rather than a global regularizer. We restrict generative supervision strictly to the underdetermined high-frequency subspace. We define a projection operator P_H :

$$P_H(x) = \mathcal{F}^{-1}(\mathbf{h} \cdot \mathcal{F}(x))$$

where \mathcal{F} and \mathcal{F}^{-1} denote the Fourier transform and its inverse, and \mathbf{h} is a radial high-pass filter mask defined as,

$$\mathbf{h}(u, v) = \text{clip} \left[\left[\left(\frac{\alpha u}{R} \right)^2 + \left(\frac{\alpha v}{R} \right)^2 \right]^\gamma + \beta, 0, 1 \right],$$

where (u, v) are frequency coordinates, R is half the maximum frequency, α, γ are scaling factors, and β is a bias term. We employ a fixed, smooth radial high-pass mask h to avoid spatial ringing artifacts (Gibbs phenomenon) and ensure stable optimization. The cutoff is set to a moderate fraction of the Nyquist frequency. This choice reflects the empirical observation that burst alignment and fusion reliably recover coarse and mid-frequency structure, while the highest frequencies remain the most sensitive to noise and sampling limitations. Importantly, our objective is not to precisely estimate the exact null space of the forward operator, but simply to attenuate generative gradients in frequency bands where the sensor likelihood is already

strong. In practice, we found that a moderate, smooth cutoff achieves stable training without requiring heuristic hyperparameter tuning.

Crucially, we project the score gradients rather than masking the image content itself. Naive VSD modifies both observable and unobservable components indiscriminately. By applying P_H , we reformulate the update:

$$\nabla_{\mathbf{x}} \mathcal{L}_{HF-VSD} = P_H(\nabla_{\mathbf{x}} \mathcal{L}_{VSD})$$

This projection ensures that the generative prior’s gradient updates are restricted to the orthogonal complement of the highly observable subspace. Consequently, it preserves the null space of the data operator; the low-frequency structure is mainly governed by data fidelity (\mathcal{L}_{data}), while the generative prior synthesizes only the missing fine-scale textures. This regularization can be converted to a loss function to train our model as,

$$\mathcal{L}_{HF-VSD}(\hat{\mathbf{x}}) = \mathbb{E}_{t, \epsilon} [\mathcal{L}_{MSE}[z_t, \delta z_t]] \quad (2)$$

where,

$$\delta z_t = z_t - P_H(\omega(t)[\Omega_{\phi'}(\hat{z}_t; t, c) - \Omega_{\phi}(\hat{z}_t; t, c)]),$$

and $\omega(t)$ is a weighting factor. This loss formulation is equivalent to minimizing the L_2 norm of the masked gradient difference, effectively ignoring errors in the low-frequency regions and focusing the generator’s updates on creating fine details. Hence, the final loss for updating the generator G_θ is the weighted sum of the data fidelity and regularization terms: $\mathcal{L}_{total} = \mathcal{L}_{data} + \lambda \mathcal{L}_{HF-VSD}$ where λ controls the strength of the generative regularization.

Theoretical Grounding: From a Bayesian perspective, restoring the high-resolution image x from burst measurements y requires maximizing the posterior score: $\nabla_x \log p(x|y) = \nabla_x \log p(y|x) + \nabla_x \log p(x)$. In heavily ill-posed inverse problems, the forward operator A (modeling optical blur, downsampling, and mosaicing) possesses a pronounced null space. The data likelihood score $\nabla_x \log p(y|x)$ strongly constrains the range space of A (the observable low frequencies) but provides zero information in the null space (the unobservable high frequencies).

A standard generative prior $\nabla_x \log p(x)$ operates over the entire space. However, because our prior is distilled from an sRGB-trained diffusion model, its low-frequency distribution fundamentally diverges from the linear RAW sensor distribution. Allowing the prior to update the range space introduces a direct mathematical conflict with the data likelihood. HF-VSD resolves this by applying a projection operator P_H to the score gradient. By restricting the prior update to $P_H \nabla_x \log p(x)$, we explicitly constrain the generative prior to act only within the effective null space of the measurement operator. This ensures the prior acts as a complementary regularizer rather than a competing likelihood, grounding our frequency mask in rigorous inverse problem theory.

4.3. Generative Multi-Frame Architecture

We designed an architecture that reliably estimates the observable component \mathbf{x}_L from sensor data and maps it into the latent space for generative refinement.

4.3.1. Sensor-Domain Alignment and Fusion

Accurate estimation of the low-frequency structure \mathbf{x}_L is critical before applying generative refinement. Because our inputs are handheld bursts, the frames suffer from non-rigid temporal misalignment. Rather than relying on external optical flow networks, we embed Spatial Transformer Networks (STNs) directly within the RAW-domain multi-frame encoder (Fig. 4). The STNs estimate global homographies to warp the deep feature embeddings of frames $i \in \{2 \dots N\}$ to the reference frame $i = 1$. This explicit sensor-domain alignment efficiently fuses burst data, thereby minimizing ambiguity in the observable subspace prior to the latent mapping phase. This ensures that the latent features fused by the subsequent convolutional layers are spatially coherent, maximizing the effective receptive field and preventing ghosting artifacts during the generative decoding phase.

4.3.2. Sensor-to-Latent Mapping

To leverage the subspace-restricted diffusion prior, we must bridge the gap between the physical sensor likelihood and the pretrained sRGB prior. We perform a deterministic linear channel extraction on the Bayer inputs to form a 33-channel stacked volume, preserving the radiometric linear-

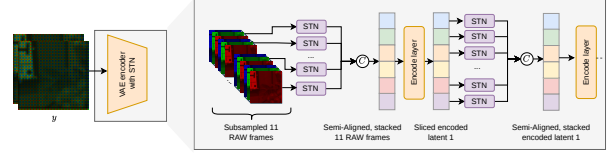


Figure 4. The architecture of the encoder that aligns the RAW frames and intermediate latents using STNs.

ity and independent noise distributions of the RAW data (see Suppl). Our STN-embedded encoder then maps this linear volume directly into the standard SD latent space. By freezing the pretrained VAE decoder, we ensure the latent space remains perfectly aligned with the diffusion prior’s expectations, allowing HF-VSD to operate effectively. We utilize a text prompt extractor, DAPE from [39], to give text embeddings to the diffusion prior.

4.4. Dataset Construction and Motion Simulation

Acquiring perfectly aligned, noise-free ground truth for genuine handheld RAW bursts is physically impossible due to the inherent temporal mismatch between a shaky short-exposure burst and the necessary long-exposure reference. To construct a rigorous paired dataset, we capture static tripod scenes to obtain pristine, long-exposure ground-truth RGB images alongside their corresponding short-exposure RAW pairs, natively preserving realistic Poisson-Gaussian sensor noise. We used a Samsung Galaxy S23 Ultra’s Wide Camera to capture 3000 burst RAW scenes and extract them after lens shading correction, white balancing, and black level subtraction, but before any ISP denoising, to ensure that the captured RAW frames contain realistic noise before demosaicing, which is not perfectly achievable using synthetic datasets that simulate RAW images from RGB images. The dataset includes low-light and bright light captures ranging from ISO 500 to 2400. The content is static and includes indoor and outdoor scenes from homes, supermarkets, and public spaces.

To simulate handheld motion without introducing the domain gaps typical of purely synthetic affine warps, we adopt an empirical simulation strategy. We extract continuous inter-frame homography trajectories from a separate dataset of real handheld bursts [16] and apply these real-world motion paths to our static RAW captures. This ensures our network learns to align physically accurate, temporally correlated hand tremors while still allowing us to evaluate the generative output against mathematically perfect ground truth. Finally, to simulate resolution loss, we utilize a Bayer-preserving Space-to-Depth downsampling operation. Comprehensive capture logistics and hardware details are provided in the Supplementary Material.

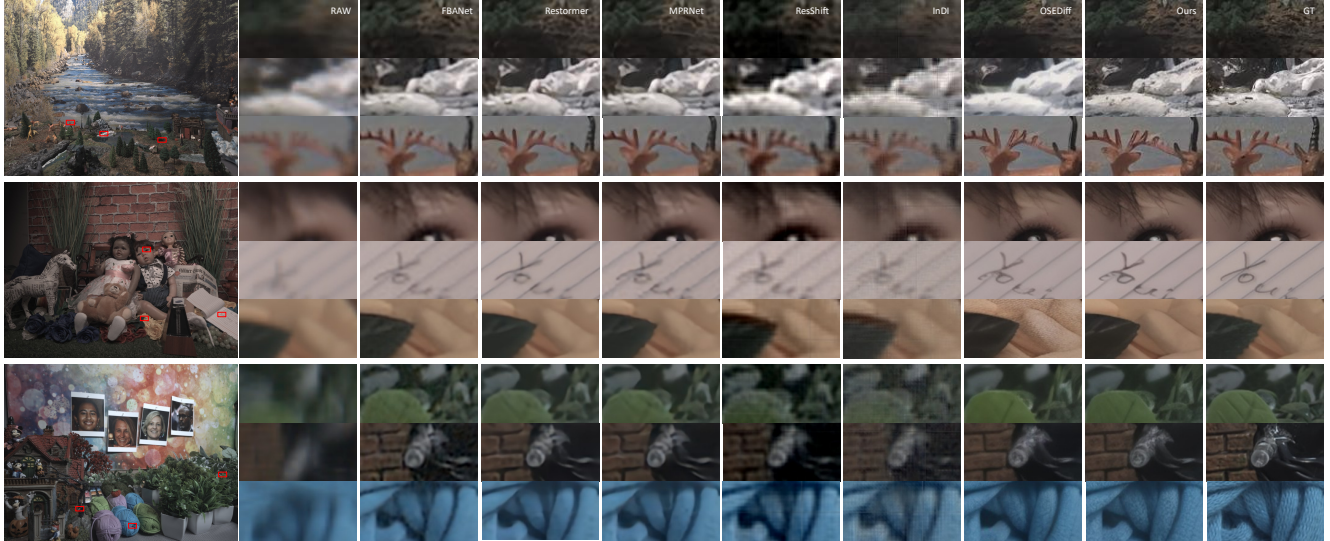


Figure 5. Qualitative comparison of different postprocessing algorithms for generating RGB images using multi-frame RAW as input. Our algorithm produces finer details in the reconstructed RGB image than all baselines and also exhibits stability in the low-frequency range.

Figure 6. Comparison of methods for the $4\times$ super-resolution using fidelity (PSNR, SSIM), perception quality (LPIPS, DISTS, FID), and no-reference quality (NIQE, MUSIQ, MANIQA, CLIPIQA) metrics. The methods are grouped into non-diffusion-based and diffusion-based approaches to highlight their different training strategies. We highlight the **best**, **second-best**, and **third-best** values for each metric.

Method	PSNR \uparrow	SSIM \uparrow	LPIPS \downarrow	DISTS \downarrow	FID \downarrow	NIQE \downarrow	MUSIQ \uparrow	MANIQA \uparrow	CLIPIQA \uparrow
Reference	29.87	0.8841	0.3018	0.2512	39.41	9.6690	23.40	0.3160	0.4502
FBANet[36]	30.88	0.9341	0.1891	0.1354	21.74	6.5970	34.53	0.3153	0.4864
Burstormer[10]	35.07	0.9454	0.0948	0.0669	12.32	5.5131	36.72	0.3450	0.3600
MPRNet[42]	35.18	0.9471	0.1309	0.1045	21.51	6.9476	38.93	0.3540	0.4471
Restormer [41]	35.24	0.9522	0.1172	0.0967	16.10	7.0328	39.09	0.3570	0.4409
ResShift [40]	26.12	0.8623	0.2927	0.1760	41.82	6.1530	29.32	0.3079	0.3429
InDI [7]	32.69	0.8987	0.2486	0.2134	57.12	5.4929	28.41	0.3162	0.3207
VSD [38]	29.75	0.9019	0.1232	0.0733	20.02	5.2592	39.08	0.3621	0.3935
Ours (no HF loss)	29.78	0.8998	0.1131	0.0662	18.58	5.1981	38.26	0.3631	0.4081
Ours	32.51	0.9200	0.0984	0.0585	14.22	5.1912	39.20	0.3643	0.4184

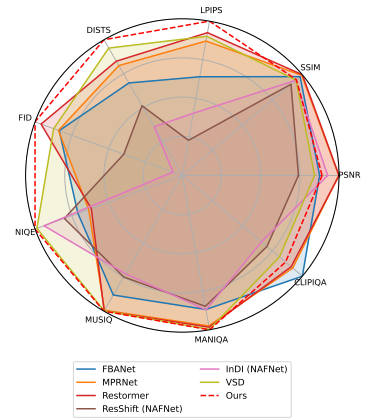


Figure 7. Performance comparison with selected competing baselines.

5. Experiments

We evaluate the proposed framework along three axes: reconstruction fidelity, perceptual realism, and structural consistency under generative regularization. We compare our method against state-of-the-art multi-frame super-resolution restoration models, including both regression-based and generative approaches. We report standard distortion metrics (PSNR, SSIM) and perceptual metrics (LPIPS[44] and FID[13]) and conduct a controlled user study to assess visual preference. We use PSNR and SSIM as pixel-based metrics to assess restoration fidelity relative to the ground truth. In addition, we perform targeted ablations to isolate the effect of High-Frequency Variational Score Distillation (HF-VSD), the alignment module, and

generative prior adaptation. See Suppl. for training details.

Comparison with baselines: We trained a set of baseline methods with our data after making minimal changes to their architectures to accommodate multi-frame RAW input. A major novelty of our pipeline is the adaptation of single-frame generative architectures to multi-frame RAW bursts. Standard diffusion models and restoration baselines (e.g., OSEDiff, NAFNet) accept 3-channel RGB inputs. To process Bayer RAW bursts, we pack the sub-sampled RAW frames into a 3-channel format and concatenated all 11 frames to create a 33-channel input requiring the initial convolutional layers of both our encoder and the retrained baselines to accept a 33-channel input. By modifying these initial projection layers and adjusting subsequent layers to ensure smooth variation of channel dimension with mini-

Table 1. Comparison of proposed method with single-frame baselines for 4× SR case.

Method	LPIPS	FID	PSNR	SSIM
GAN (SF NAFNet)	0.13	9.53	28.18	0.86
VSD (SF)	0.14	16.53	28.67	0.87
Ours (MF)	0.09	14.22	31.43	0.90

mal changes to the underlying architecture of the baselines. By retraining all models from scratch, we ensure that the network can natively fuse temporal sub-pixel information across the 33 channels to produce the final RGB output.

We compare our method with state-of-the-art generative models for image restoration, namely, ResShift [40], InDI [7], and OSediff [38], and some adversarially-trained models such as Burstormer [10], MPRNet[42] and Restormer [41]. The quantitative results for these baselines are given in Fig. 6. Our method achieves the best generative quality metrics among competing methods. Although adversarially trained methods yield better metrics, our method qualitatively demonstrates superior generative capability, as illustrated in Fig. 5, where it can reconstruct plausible, realistic high-frequency details.

The Perception-Distortion Trade-off in Burst SR. As shown in Table 6, deterministic regression baselines (e.g., Restormer, MPRNet) achieve higher PSNR (e.g., ~35 dB) compared to our generative framework (~32.5 dB). Rather than a limitation, this quantitative gap perfectly illustrates the core theoretical trade-off of our formulation. Because regression baselines minimize Mean Squared Error (MSE), they mathematically converge to the posterior distribution’s mean. While this maximizes PSNR, it heavily penalizes high-frequency variance, resulting in the overly smooth or “waxy” textures observed in Fig. 5. In contrast, GenMFSR is explicitly designed to sample a specific, stochastic realization from the posterior to recover photorealistic texture. As established by the Perception-Distortion trade-off [1], this stochasticity guarantees a drop in pixel-wise distortion metrics like PSNR in exchange for superior perceptual quality. By optimizing for distributional alignment via HF-VSD, GenMFSR achieves state-of-the-art LPIPS and FID scores.

Details of User Study: Due to the limitations of traditional image quality metrics in capturing user perception, we conducted a user study to evaluate the proposed method. Twenty-two image quality experts were shown the outputs of the NAFNET trained with a GAN, the baseline VSD method, and our proposed GenMFSR method on 30 randomly selected crops from the test set. For each crop, subjects were asked to choose the preferred image or indicate whether the images looked the same. As shown in Fig. 8, a plurality of experts preferred images generated by our

Table 2. Comparisons of Params and FLOPs between GenMFSR and its competing methods on input resolution of 512 × 512.

Method	Type	Params (M)	FLOPs (G)
FBANet [36]	CNN	~28.5	~120
Burstormer [10]	Transformer	3.58	613
MPRNet [42]	CNN	20	595
Restormer [41]	Transformer	26.1	567
ResShift [40]	15-step Diffusion	119	5500
InDI [7]	50-step Diffusion	54	48000
VSD (OSediff) [38]	1-step Diffusion	1775.0	4530
Ours (GenMFSR)	1-step Diffusion	1310.0	4620

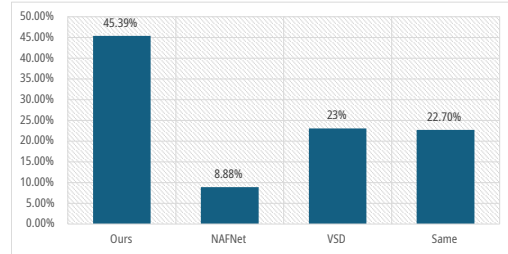


Figure 8. A survey of 22 image quality experts shows a strong perceptual preference for our method (45.39%). Despite its high quantitative metrics, the GAN-based NAFNet was strongly disfavored (8.88%) due to artifacts, demonstrating the gap between standard metrics and human perception.



Figure 9. Comparison of our method after training on single-frame and multi-frame RAW images. This shows the need for multiple frames in the RAW-to-RGB problem.

method. The post-study feedback indicated that the artifacts in the NAFNet were the primary reason it was not preferred, and the lack of detail in the baseline VSD method was also a contributing factor to its non-preference. Some examples of the artifacts produced by the NAFNET are shown in Fig. 5. These crosshatch patterns may be an outcome of the network learning to game loss terms such as L1, GAN, and LPIPS, which is a well-known phenomenon known as perception-fidelity tradeoff [1].

Single Frame vs Multi-Frame: We also experimentally validate the benefit of using multiple frames by using only the RAW base frame and GT pairs to train single-frame baselines. The comparison with these baselines is presented in Tab. 1, which shows that our multi-frame ap-

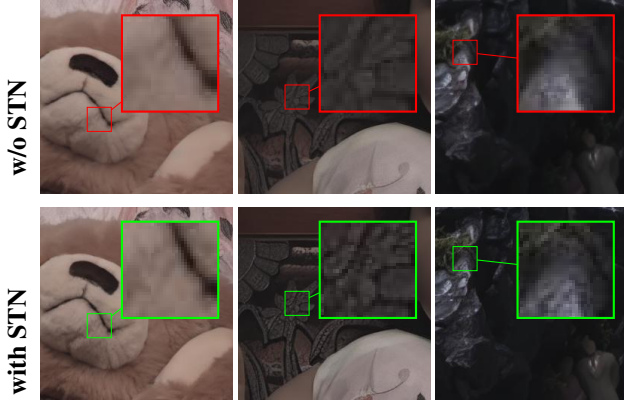


Figure 10. Ablation study showing the effectiveness of using STNs without utilizing the HF loss for a fair comparison of the encoder stage. When STNs are used in the encoder, the overall sharpness of the images is improved since all frames are aligned.

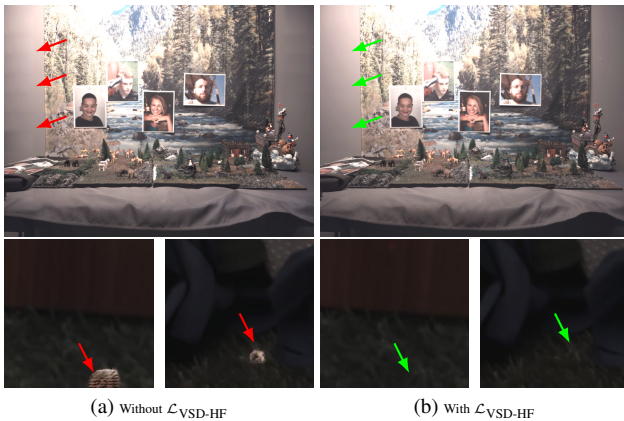


Figure 11. Effectiveness of the high-frequency (HF) VSD loss. Both models use STNs for alignment. (a) The baseline VSD introduces low-frequency patching artifacts (top, contrast enhanced) and hallucinations (bottom). (b) Our \mathcal{L}_{VSD-HF} successfully prevents both types of artifacts.

proach outperforms all single-frame RAW-to-RGB methods. A qualitative comparison in Fig. 9 shows that GenMFSR has greater fidelity than single-frame methods.

Deployment and Practicality. We note that deploying a 1.3B parameter latent diffusion model is impractical for real-time, viewfinder-level mobile processing (e.g., 30 fps). Consequently, GenMFSR is designed to operate as an *Asynchronous Enhancement Module*, akin to premium computational photography pipelines (e.g., Deep Fusion or Night Sight) that process high-fidelity bursts in the background post-capture. By utilizing one-step distillation, our framework reduces the latency of standard diffusion from dozens of seconds to a single forward pass, making high-end generative burst restoration practically viable for mod-

ern mobile Neural Processing Units (NPUs). Further distillation and mobile deployment is made possible by recent works[23, 29].

6. Ablation study

We trained the proposed network without using STN blocks in the encoder to verify the performance gain from using STNs. Fig. 10 illustrates how the addition of STNs produces sharper images in the final reconstruction. This validates the efficacy of using STNs for image registration in the encoder stage, aligning the frames and making the subsequent tasks easier for the generative network.

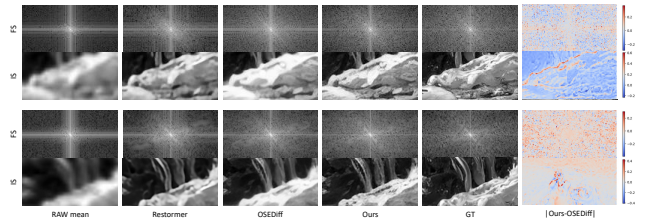


Figure 12. Comparison of competing results in the Frequency Space (FS) and Image Space (IS). We highlight the absolute error between ours and OSEDiff [38] which is a close competing method.

Furthermore, Fig. 11 demonstrates that restricting the generative prior ensures low-frequency uniformity across patches. This explicitly prevents the severe boundary artifacts (top row) and structural hallucinations (bottom row) that plague the unconstrained baseline VSD.

Fourier spectra analysis Fig. 12 confirms naive VSD alters low-frequency magnitudes, causing the color shifts and hallucinations as shown in Fig. 11. Conversely, GenMFSR matches the ground-truth low-frequency spectrum while extrapolating high-frequency bounds, thereby reducing low-frequency structural error compared to standard VSD. Fig. 12 also highlights the difference between OSEDiff [38] and our method in the image space and frequency space where ours shows improvements in edges and high frequency components. This confirms that our subspace projection successfully bridges the RAW-to-RGB domain gap, recovering the critical sub-pixel textures lost by standard regression models without triggering the severe structural drift inherent to unconstrained diffusion priors.

7. Conclusion

We introduced GenMFSR, the first unified, one-step generative framework for multi-frame RAW-to-RGB restoration. By embedding explicit frame alignment within the encoder and restricting generative priors to the high-frequency latent subspace, GenMFSR successfully synthesizes photorealistic sub-pixel details without structural hallucinations. This

offers a highly effective, sensor-stage architecture for modern mobile ISPs. Because the framework relies on a frozen Stable Diffusion prior to bypassing heavy training costs, it naturally inherits the foundation model’s constraints, such as minor global color shifts or VAE-induced text artifacts. Future work will explore rectified flow and global foveal context to refine patch-based prompting, further bridging the gap between powerful generative priors and physical sensor constraints.

References

- [1] Yochai Blau and Tomer Michaeli. The perception-distortion tradeoff. In *Proceedings of the IEEE/CVF conference on computer vision and pattern recognition*, pages 6228–6237, 2018.
- [2] Ryan Burgert, Yuancheng Xu, Wenqi Xian, Oliver Pilarski, Pascal Clausen, Mingming He, Li Ma, Yitong Deng, Lingxiao Li, Mohsen Mousavi, et al. Go-with-the-flow: Motion-controllable video diffusion models using real-time warped noise. In *Proceedings of the IEEE/CVF international conference on computer vision*, pages 13–23, 2025.
- [3] Liangyu Chen, Xiaojie Chu, Xiangyu Zhang, and Jian Sun. Simple baselines for image restoration. In *European conference on computer vision*, pages 17–33. Springer, 2022.
- [4] Yan Chen, Yi Wen, Wei Li, Junchao Liu, Yong Guo, Jie Hu, and Xinghao Chen. Rddm: Practicing raw domain diffusion model for real-world image restoration. *arXiv preprint arXiv:2508.19154*, 2025.
- [5] Jifeng Dai, Haozhi Qi, Yuwen Xiong, Yi Li, Guodong Zhang, Han Hu, and Yichen Wei. Deformable convolutional networks. In *Proceedings of the IEEE international conference on computer vision*, pages 764–773, 2017.
- [6] Longquan Dai, He Wang, and Jinhui Tang. Noisectrl: A sampling-algorithm-agnostic conditional generation method for diffusion models. In *Proceedings of the IEEE/CVF conference on computer vision and pattern recognition*, pages 18093–18102, 2025.
- [7] Mauricio Delbracio and Peyman Milanfar. Inversion by direct iteration: An alternative to denoising diffusion for image restoration. *arXiv preprint arXiv:2303.11435*, 2023.
- [8] Zheng-Peng Duan, Jiawei Zhang, Xin Jin, Ziheng Zhang, Zheng Xiong, Dongqing Zou, Jimmy S Ren, Chunle Guo, and Chongyi Li. Dit4sr: Taming diffusion transformer for real-world image super-resolution. In *Proceedings of the IEEE/CVF International Conference on Computer Vision*, pages 18948–18958, 2025.
- [9] Akshay Dudhane, Syed Waqas Zamir, Salman Khan, Fahad Shahbaz Khan, and Ming-Hsuan Yang. Burst image restoration and enhancement. In *Proceedings of the IEEE/CVF Conference on Computer Vision and Pattern Recognition*, pages 5759–5768, 2022.
- [10] Akshay Dudhane, Syed Waqas Zamir, Salman Khan, Fahad Shahbaz Khan, and Ming-Hsuan Yang. Burstformer: Burst image restoration and enhancement transformer. In *Proceedings of the IEEE/CVF conference on computer vision and pattern recognition*, pages 5703–5712. IEEE, 2023.
- [11] Patrick Esser, Johnathan Chiu, Parmida Atighehchian, Jonathan Granskog, and Anastasis Germanidis. Structure and content-guided video synthesis with diffusion models. In *Proceedings of the IEEE/CVF international conference on computer vision*, pages 7346–7356, 2023.
- [12] Sina Farsiu, M Dirk Robinson, Michael Elad, and Peyman Milanfar. Fast and robust multiframe super resolution. *IEEE transactions on image processing*, 13(10):1327–1344, 2004.
- [13] Martin Heusel, Hubert Ramsauer, Thomas Unterthiner, Bernhard Nessler, and Sepp Hochreiter. Gans trained by a two time-scale update rule converge to a local nash equilibrium. *Advances in neural information processing systems*, 30, 2017.
- [14] Edward J Hu, Yelong Shen, Phillip Wallis, Zeyuan Allen-Zhu, Yuanzhi Li, Shean Wang, Lu Wang, Weizhu Chen, et al. Lora: Low-rank adaptation of large language models. *International Conference on Learning Representations (ICLR)*, 1(2):3, 2022.
- [15] Max Jaderberg, Karen Simonyan, Andrew Zisserman, et al. Spatial transformer networks. *Advances in neural information processing systems*, 28, 2015.
- [16] Fadeel Sher Khan, Joshua Ebenezer, Hamid Sheikh, and Seok-Jun Lee. Mfsr-gan: Multi-frame super-resolution with handheld motion modeling. In *Proceedings of the IEEE/CVF conference on computer vision and pattern recognition*, pages 800–809, 2025.
- [17] Zongyi Li, Nikola Kovachki, Kamyar Aizzadenesheli, Burigede Liu, Kaushik Bhattacharya, Andrew Stuart, and Anima Anandkumar. Fourier neural operator for parametric partial differential equations. *arXiv preprint arXiv:2010.08895*, 2020.
- [18] Xinqi Lin, Jingwen He, Ziyang Chen, Zhaoyang Lyu, Bo Dai, Fanghua Yu, Yu Qiao, Wanli Ouyang, and Chao Dong. Diffbir: Toward blind image restoration with generative diffusion prior. In *European conference on computer vision*, pages 430–448. Springer, 2024.
- [19] Ze Liu, Yutong Lin, Yue Cao, Han Hu, Yixuan Wei, Zheng Zhang, Stephen Lin, and Baining Guo. Swin transformer: Hierarchical vision transformer using shifted windows. In *Proceedings of the IEEE/CVF international conference on computer vision*, pages 10012–10022, 2021.
- [20] Eric Luhman and Troy Luhman. Knowledge distillation in iterative generative models for improved sampling speed. *arXiv preprint arXiv:2101.02388*, 2021.
- [21] Chenlin Meng, Robin Rombach, Ruiqi Gao, Diederik Kingma, Stefano Ermon, Jonathan Ho, and Tim Salimans. On distillation of guided diffusion models. In *Proceedings of the IEEE/CVF conference on computer vision and pattern recognition*, pages 14297–14306, 2023.
- [22] Chong Mou, Xintao Wang, Liangbin Xie, Yanze Wu, Jian Zhang, Zhongang Qi, and Ying Shan. T2i-adapter: Learning adapters to dig out more controllable ability for text-to-image diffusion models. In *Proceedings of the AAAI conference on artificial intelligence*, volume 38, pages 4296–4304, 2024.
- [23] Mehdi Noroozi, Isma Hadji, Victor Escorcia, Anestis Zaganidis, Brais Martinez, and Georgios Tzimiropoulos. Edgesd-sr: Low latency and parameter efficient on-device super-resolution with stable diffusion via bidirectional conditioning. *arXiv preprint arXiv:2412.06978*, 2024.
- [24] Ben Poole, Ajay Jain, Jonathan T Barron, and Ben Mildenhall.

- hall. Dreamfusion: Text-to-3d using 2d diffusion. *arXiv preprint arXiv:2209.14988*, 2022.
- [25] Yang Ren, Hai Jiang, Menglong Yang, Wei Li, and Shuaicheng Liu. Ispdiffuser: Learning raw-to-srgb mappings with texture-aware diffusion models and histogram-guided color consistency. In *Proceedings of the AAAI Conference on Artificial Intelligence*, volume 39, pages 6722–6730, 2025.
- [26] Robin Rombach, Andreas Blattmann, Dominik Lorenz, Patrick Esser, and Björn Ommer. High-resolution image synthesis with latent diffusion models, 2021.
- [27] Robin Rombach, Andreas Blattmann, Dominik Lorenz, Patrick Esser, and Björn Ommer. High-resolution image synthesis with latent diffusion models. In *Proceedings of the IEEE/CVF conference on computer vision and pattern recognition*, pages 10684–10695, 2022.
- [28] Tim Salimans and Jonathan Ho. Progressive distillation for fast sampling of diffusion models. *arXiv preprint arXiv:2202.00512*, 2022.
- [29] Subhajit Sanyal, Srinivas Soumitri Miriyala, Akshay Janardan Bankar, Sravanth Kodavanti, Abhishek Ameta, Shreyas Pandith, Amit Satish Unde, et al. Nanosd: Edge efficient foundation model for real time image restoration. *arXiv preprint arXiv:2601.09823*, 2026.
- [30] Jiaming Song, Chenlin Meng, and Stefano Ermon. Denoising diffusion implicit models. In *International Conference on Learning Representations*, 2021.
- [31] Yang Song, Prafulla Dhariwal, Mark Chen, and Ilya Sutskever. Consistency models, 2023.
- [32] Lingchen Sun, Rongyuan Wu, Zhiyuan Ma, Shuaizheng Liu, Qiaosi Yi, and Lei Zhang. Pixel-level and semantic-level adjustable super-resolution: A dual-lora approach. In *Proceedings of the Computer Vision and Pattern Recognition Conference*, pages 2333–2343, 2025.
- [33] Jiangshan Wang, Junfu Pu, Zhongang Qi, Jiayi Guo, Yue Ma, Nisha Huang, Yuxin Chen, Xiu Li, and Ying Shan. Taming rectified flow for inversion and editing. *arXiv preprint arXiv:2411.04746*, 2024.
- [34] Yinhuai Wang, Jiwen Yu, and Jian Zhang. Zero-shot image restoration using denoising diffusion null-space model. *arXiv preprint arXiv:2212.00490*, 2022.
- [35] Zhengyi Wang, Cheng Lu, Yikai Wang, Fan Bao, Chongxuan Li, Hang Su, and Jun Zhu. Prolificdreamer: High-fidelity and diverse text-to-3d generation with variational score distillation. *Advances in neural information processing systems*, 36:8406–8441, 2023.
- [36] Pengxu Wei, Yujing Sun, Xingbei Guo, Chang Liu, Guanbin Li, Jie Chen, Xiangyang Ji, and Liang Lin. Towards real-world burst image super-resolution: Benchmark and method. In *Proceedings of the IEEE/CVF international conference on computer vision*, pages 13233–13242, 2023.
- [37] Bartłomiej Wronski, Ignacio Garcia-Dorado, Manfred Ernst, Damien Kelly, Michael Krainin, Chia-Kai Liang, Marc Levoy, and Peyman Milanfar. Handheld multi-frame super-resolution. *ACM Transactions on Graphics (ToG)*, 38(4):1–18, 2019.
- [38] Rongyuan Wu, Lingchen Sun, Zhiyuan Ma, and Lei Zhang. One-step effective diffusion network for real-world image super-resolution. *Advances in Neural Information Processing Systems*, 37:92529–92553, 2024.
- [39] Rongyuan Wu, Tao Yang, Lingchen Sun, Zhengqiang Zhang, Shuai Li, and Lei Zhang. Seesr: Towards semantics-aware real-world image super-resolution. In *Proceedings of the IEEE/CVF conference on computer vision and pattern recognition*, pages 25456–25467, 2024.
- [40] Zongsheng Yue, Jianyi Wang, and Chen Change Loy. Resshift: Efficient diffusion model for image super-resolution by residual shifting. *Advances in Neural Information Processing Systems*, 36:13294–13307, 2023.
- [41] Syed Waqas Zamir, Aditya Arora, Salman Khan, Munawar Hayat, Fahad Shahbaz Khan, and Ming-Hsuan Yang. Restormer: Efficient transformer for high-resolution image restoration. In *Proceedings of the IEEE/CVF conference on computer vision and pattern recognition*, pages 5728–5739, 2022.
- [42] Syed Waqas Zamir, Aditya Arora, Salman Khan, Munawar Hayat, Fahad Shahbaz Khan, Ming-Hsuan Yang, and Ling Shao. Multi-stage progressive image restoration. In *Proceedings of the IEEE/CVF conference on computer vision and pattern recognition*, pages 14821–14831, 2021.
- [43] Lvmin Zhang, Anyi Rao, and Maneesh Agrawala. Adding conditional control to text-to-image diffusion models. In *Proceedings of the IEEE/CVF international conference on computer vision*, pages 3836–3847, 2023.
- [44] Richard Zhang, Phillip Isola, Alexei A Efros, Eli Shechtman, and Oliver Wang. The unreasonable effectiveness of deep features as a perceptual metric. In *Proceedings of the IEEE/CVF conference on computer vision and pattern recognition*, pages 586–595, 2018.
- [45] Amber Yijia Zheng, Yu Zhang, Jun Hu, Raymond A Yeh, and Chen Chen. Darkdiff: Advancing low-light raw enhancement by retasking diffusion models for camera isp. *arXiv preprint arXiv:2505.23743*, 2025.

GenMFSR: Generative Multi-Frame Image Restoration and Super-Resolution

Supplementary Material

A. Introduction

This supplementary material provides a theoretical background on score distillation and how it is related to high-frequency feature generation, more information on model training and the dataset in Sec. C. Additional experiment results are presented in Sec. D, including qualitative results that demonstrate super-resolution scaling agnosticism and perceptual quality improvements over adversarial Networks (GANs). We provide further details of the user study, along with some examples of the images used in Sec. E.

B. Theoretical background

B.1. Variational Score Distillation (VSD)

VSD works by minimizing the KL divergence $\mathcal{D}_{\text{KL}}(q_{\theta}(\hat{\mathbf{z}})||p(\mathbf{z}))$ between the distribution of noisy predicted latents $\hat{\mathbf{z}}$ and noisy real latents \mathbf{z} , denoted by q_{θ} and p respectively. This can be implemented using techniques such as adversarial training, where a discriminator is trained to identify p and q_{θ} . The goal of the generator is to predict $\hat{\mathbf{x}}$ such that $q_{\theta} \simeq p$, which reduces the KL divergence. This will regularize the generator to produce images that are close to the ground-truth distribution. However, according to the authors of VSD [35], the distribution of \mathbf{z} can be sparse, which may yield suboptimal results.

But if we add noise to these latent variables ($\hat{\mathbf{z}}_t = \alpha_t \hat{\mathbf{z}} + \beta_t \epsilon_t$), we can diffuse the distributions to easily calculate a valid KL divergence $\mathcal{D}_{\text{KL}}(q_{\theta,t}(\hat{\mathbf{z}}_t)||p_t(\mathbf{z}_t))$ where t is the time step, $\epsilon \in \mathcal{N}(0, \mathbf{I})$, and α_t, β_t are noise schedule coefficients. This tractable problem can be written as,

$$\theta^* = \arg \min_{\theta} \mathbb{E}_t[(\alpha_t/\beta_t)\omega(t)\mathcal{D}_{\text{KL}}(q_{\theta,t}(\hat{\mathbf{z}}_t)||p_t(\mathbf{z}_t))] \quad (3)$$

where $\omega(t)$ is a weighting factor.

Since pretrained diffusion models such as Stable Diffusion already have the capability to estimate the distribution of diffused real images, we use a frozen Stable Diffusion model $\Omega_{\phi'}$ to estimate the distribution (or score function) of \mathbf{z}_t . The distribution of the predicted latents $\hat{\mathbf{z}}_t$ is estimated using another noise prediction network Ω_{ϕ} , which is trained on the predicted latents with the standard diffusion loss,

$$\mathcal{L}_{\text{diff}} = \mathbb{E}_{t,\epsilon,\hat{\mathbf{z}}}\mathcal{L}_{\text{MSE}}(\Omega_{\phi}(\alpha_t \hat{\mathbf{z}} + \beta_t \epsilon; t, \mathbf{c}), \epsilon) \quad (4)$$

Using these estimations of the distributions, we can solve the problem in Eq. (3) by calculating its gradient. For that,

we define the gradient of VSD loss as,

$$\nabla_{\hat{\mathbf{x}}}\mathcal{L}_{\text{VSD}}(\hat{\mathbf{x}}) \triangleq \mathbb{E}_{t,\epsilon} \left[\omega(t)(\Omega_{\phi'}(\mathbf{z}_t; t, \mathbf{c}) - \Omega_{\phi}(\hat{\mathbf{z}}_t; t, \mathbf{c})) \frac{\partial \mathbf{z}_t}{\partial \hat{\mathbf{x}}} \right]$$

Since the decoder is frozen, the VSD loss can be computed in the latent space. Therefore, we can update the VSD loss to backpropagate to θ as follows,

$$\begin{aligned} \nabla_{\theta}\mathcal{L}_{\text{VSD}}(\hat{\mathbf{x}}) &= \nabla_{\hat{\mathbf{x}}}\mathcal{L}_{\text{VSD}}(\hat{\mathbf{x}}) \frac{\partial \hat{\mathbf{x}}}{\partial \theta} \\ &= \mathbb{E}_{t,\epsilon} \left[\omega(t)(\Omega_{\phi'}(\mathbf{z}_t; t, \mathbf{c}) - \Omega_{\phi}(\hat{\mathbf{z}}_t; t, \mathbf{c})) \frac{\partial \mathbf{z}_t}{\partial \theta} \right] \end{aligned}$$

When we know the gradient of the loss, we can find the global minima by setting the gradient to zero, assuming the loss is convex. Therefore, VSD loss can be incorporated into training as follows,

$$\tilde{\mathcal{L}}_{\text{VSD}}(\hat{\mathbf{x}}) = \mathcal{L}_{\text{MSE}}[\omega(t)\Omega_{\phi'}(\mathbf{z}_t; t, \mathbf{c}), \omega(t)\Omega_{\phi}(\hat{\mathbf{z}}_t; t, \mathbf{c})] \quad (6)$$

B.2. HF-VSD via Null-Space Projection

We can formulate the RAW-to-RGB multi-frame super-resolution task as a linear inverse problem:

$$y = Ax + n \quad (7)$$

where $x \in \mathbb{R}^D$ is the ground-truth high-resolution RGB image, $y \in \mathbb{R}^d$ ($d \ll D$) represents the degraded RAW burst measurements, A is the forward degradation operator (blur, downsampling, mosaicing), and n is sensor noise.

To sample from the posterior $p(x|y)$, score-based generative models utilize Langevin dynamics, which requires the posterior score:

$$\nabla_x \log p(x|y) = \underbrace{\nabla_x \log p(y|x)}_{\text{Likelihood Score}} + \underbrace{\nabla_x \log p(x)}_{\text{Prior Score}} \quad (8)$$

The forward operator A induces a decomposition of the image space into a range space (observable subspace) and a null space (unobservable subspace). Let A^{\dagger} be the pseudo-inverse of A . We can define the orthogonal projection matrices for the range space $P_L = A^{\dagger}A$ and the null space $P_H = I - A^{\dagger}A$.

Any image can be decomposed as $x = P_L x + P_H x$. The likelihood score $\nabla_x \log p(y|x)$ only provides gradients for the observable subspace $P_L x$. The prior score $\nabla_x \log p(x)$ provides gradients for both subspaces.

In our framework, the prior $p(x)$ is parameterized by an sRGB-trained latent diffusion model, while y resides in the

linear RAW domain. Consequently, the prior’s score in the observable subspace, $P_L \nabla_x \log p(x)$, is heavily biased by sRGB tone-mapping and color processing, conflicting with the true physical measurements y .

To prevent this domain collision, we construct a modified posterior score that strictly isolates the prior to the null space:

$$\nabla_x \log \tilde{p}(x|y) = \nabla_x \log p(y|x) + P_H \nabla_x \log p(x) \quad (9)$$

In the spatial frequency domain, the degradation operator A behaves as a low-pass filter. Therefore, the range space P_L corresponds to low spatial frequencies, and the null space P_H corresponds to high spatial frequencies.

By applying a high-pass Fourier mask h to the gradients of the Variational Score Distillation (VSD) loss, our proposed HF-VSD acts as an efficient, differentiable approximation of the null-space projection P_H :

$$\nabla_x \mathcal{L}_{HF-VSD} \approx P_H \nabla_x \log p(x) \quad (10)$$

which can be calculated using Eq. (2). This demonstrates that HF-VSD is not a heuristic image-space filter, but a theoretically grounded technique to enforce complementary score matching in partially observable inverse problems.

Computing the exact null-space projection $P_H = I - A^\dagger A$ is computationally intractable for high-resolution images within a latent diffusion framework due to the massive dimensionality of A and the non-rigid alignment modeled by our STNs.

However, if we locally approximate A as a spatially invariant blur operator combined with uniform sampling, A represents a discrete convolution. Under circular boundary conditions, A is a Block-Circulant with Circulant Blocks (BCCB) matrix.

A fundamental property of BCCB matrices is that they are diagonalized by the 2D Discrete Fourier Transform (DFT) matrix, denoted as \mathcal{F} . Thus, we can decompose A as:

$$A = \mathcal{F}^{-1} \Lambda \mathcal{F} \quad (11)$$

where Λ is a diagonal matrix containing the Fourier coefficients of the degradation kernel (the Optical Transfer Function, OTF).

Because optical blur and pixel integration act as low-pass filters, the diagonal elements of Λ approach zero at high spatial frequencies. The pseudo-inverse projection operator onto the observable range space becomes:

$$P_L = A^\dagger A = \mathcal{F}^{-1} (\Lambda^\dagger \Lambda) \mathcal{F} \quad (12)$$

The term $(\Lambda^\dagger \Lambda)$ is a diagonal matrix with ones at low frequencies (where the signal is observable) and zeros at high frequencies (where the OTF attenuates the signal below the noise floor).

Consequently, the projection onto the unobservable null-space P_H is:

$$P_H = I - P_L = \mathcal{F}^{-1} (I - \Lambda^\dagger \Lambda) \mathcal{F} \quad (13)$$

The matrix $(I - \Lambda^\dagger \Lambda)$ is exactly a high-pass frequency mask in the Fourier domain.

Therefore, while a fixed Fourier mask h does not capture the complex, spatially varying local deformations of hand-held motion, it serves as the mathematically optimal and computationally tractable approximation of the true null-space projection for camera sensor degradations. By applying this mask to the score gradients, HF-VSD effectively restricts the generative prior to the unobservable high-frequency subspace without requiring the intractable computation of the true spatially varying pseudo-inverse.

C. Model description and training

C.1. Model details

We use the pretrained Stable Diffusion 2.1 model as the generator U-net Ω_θ and trainable regularizer $\Omega_{\phi'}$. Selected layers of these U-nets and the encoder E_θ are trained using Low Rank Adapters (LoRAs). The decoder \mathcal{D}_θ was frozen and used for decoding the reconstructed latents. The frozen regularizer $\Omega_{\phi'}$ is initialized from Stable Diffusion 2.1 and kept frozen. The high-pass filter is initialized with $\alpha = 0.8, \beta = 0.2$, and $\gamma = 4$. This filter is used in place of the Gaussian filter to provide a controllable limit on the maximum allowed high frequency.

C.2. Frame alignment for fidelity improvement.

A critical challenge in multi-frame RAW processing is temporal misalignment caused by hand tremor. Prior generative models operate on single frames and fail catastrophically when presented with misaligned bursts. To solve this, we embed Spatial Transformer Networks (STNs) directly within the multi-frame encoder E_θ . The distortion is modeled by a homography transformation relative to a base frame (e.g., the first frame). The encoder’s input layer is replaced with a convolutional layer with a channel input size of 33 to accommodate multiple RAW frames.

To accommodate the 3-channel prior of the pre-trained sRGB encoder while preserving the physical properties of the sensor data, we apply a deterministic linear channel extraction to the Bayer RAW inputs. Specifically, the Red and Blue channels are extracted and linearly upsampled ($2\times$) to the full spatial resolution. The two Green channels are similarly extracted, upsampled, and averaged. These are stacked to form a 33-channel input volume for the 11-frame burst. We explicitly note that while this constitutes a naive linear demosaicing, this 3-channel representation strictly retains the radiometric linearity, original bit-depth, and uncompressed dynamic range of the raw sensor signal. By doing so, we successfully reduce the dimensional domain gap

for the generative VAE while completely bypassing the destructive, non-linear tone-mapping, gamma correction, and heavy spatial denoising applied by standard mobile ISPs.

The trainable encoder (E_θ) and diffusion networks ($\Omega_\theta, \Omega_\phi$) are finetuned by introducing trainable LoRA [14] layers. The localization networks of Spatial Transformer Networks (STNs) [15] in E_θ are initialized to give an identity homography matrix at the start and are then trained from scratch. While training a custom RAW-domain VAE might seem intuitive, doing so would fundamentally alter the latent space, disconnecting it from the pre-trained Stable Diffusion prior. Because VSD relies on the pre-trained prior ($\Omega_{\phi'}$) to provide score estimates, our encoder must map the 33-channel RAW burst directly into the standard SD latent space. Therefore, we freeze the standard decoder D_θ and force the encoder E_θ to bridge the domain gap.

C.3. Dataset Capture and Processing Details

Hardware and Capture Logistics. We constructed an aligned dataset using registered long and short-exposure multi-frame (MF) images captured on a mobile device mounted on a tripod, ensuring strictly static scenes to eliminate unwanted camera shake. Capturing data at the beginning of the ISP pipeline ensures that the RAW frames contain authentic, sensor-specific Poisson-Gaussian noise distributions before any destructive demosaicing occurs—a property that cannot be perfectly replicated using synthetic inverse-ISP pipelines. To maintain consistent luminance across the pairs, the brightness of the short-exposure and long-exposure images was equalized by adjusting the ISO during capture. The ground-truth high-resolution (HR) RGB images were obtained by fusing and demosaicing the pristine long-exposure RAW frames, thereby minimizing noise and eliminating blur.

Continuous Motion Simulation. To simulate handheld motion without introducing the domain gaps typical of purely synthetic affine warps, we utilized a supplementary dataset of real-world handheld bursts [16]. Crucially, differing from [16] where homographies were sampled independently for each input frame, our empirical simulation extracts groups of continuous homographies from entire multi-frame captures. We apply these motion trajectories jointly to the static short-exposure frames. This modification preserves the temporal correlations inherent in actual human hand tremors, resulting in highly realistic synthetic motion sequences that accurately reflect mobile burst photography.

Data Processing and Splits. During the data loading pipeline, RAW frames and ground-truth RGB images are extracted, and the handshake motion is applied. To process the motion, the RAW frames are first subsampled and resized to the original size $H \times W$ using bilinear interpolation, followed by the application of the extracted homogra-

phy matrices. The RAW and RGB images are subsequently cropped to a patch size of 256×256 . The cropped and subsampled RAW frames are then downsampled (via a Bayer-preserving Space-to-Depth operation) and resized back to 256×256 to construct the final input volume to the model. Out of the collected dataset, 2000 distinct scenes are utilized for training, 100 for validation, and 100 for testing.

C.4. Training

The model is trained on a NVIDIA H100 GPU with a batch size of 4 for around 4 days. We used the Adam optimizer with a learning rate of $5e-5$. The LoRAs are initialized to give an identity at the beginning. The input layer to the encoder is initialized using random weights. The training procedure is outlined in Algorithm 1, where Y represents the caption generator and other modules are consistent with the notations presented in the main paper.

The dataset was split into training, validation, and test sets with a ratio of 90:5:5, and we trained our model with $\lambda = 1$, $\alpha = 0.8$, $\beta = 0.2$, and $\gamma = 4$. We used the Adam optimizer with a learning rate of 5×10^{-5} . Training was performed for 500k iterations, and the checkpoint with the best MSE+LPIPS on the validation set was selected as the final checkpoint for evaluation of all the considered methods.

C.5. Inference

We disregard the models used for regularization during the inference. Thus, to obtain the final reconstructed image, we need only Ω_θ , E_θ , and D_θ modules. The inference procedure is given in Algorithm 2.

D. Additional experiments

D.1. Inference-Time Scale Agnosticism:

We discussed the primary results for the $4\times$ SR case in Fig. 6. However, our model is not restricted to a fixed SR scale factor. To demonstrate this scale-agnostic capability, we illustrate qualitative results in Fig. 13, and further details are given in the supplementary material, where our method again shows the best fidelity compared to the competing generative baselines. The illustration in Fig. 13 further supports this statement by demonstrating improved texture generation from our method compared to GANs, particularly in the higher frequencies.

D.2. Comparison with related works

In addition to the qualitative comparison methods given in the main paper, we show the qualitative results from BIPNet [9], FBANet [36], MPRNet [42], Restormer [41], Burstormer [10], and ResShift [40] in Fig. 14 and Fig. 15.

Algorithm 1 Training Procedure

Load pretrained $\Omega_{\phi'}$, E_{θ} , D_{θ} , Y
Copy weights Ω_{θ} , Ω_{ϕ} \leftarrow $\Omega_{\phi'}$
Initialize LoRA on Ω_{θ} , Ω_{ϕ} , E_{θ}
Initialize STNs on E_{θ}

- 1: **procedure** TRAIN(Dataset $\mathcal{D}_{\text{train}}$)
- 2: **for** i from 0 to N **do**
- 3: $\mathbf{y}, \mathbf{x} \sim \mathcal{D}_{\text{train}}$
- 4: $c \leftarrow Y(\mathbf{y})$
- 5: $\mathbf{z}_T \leftarrow E_{\theta}(\mathbf{y})$ \triangleright Encoding with alignment
- 6: $\hat{\mathbf{v}}_0 \leftarrow \Omega_{\theta}(\mathbf{z}_T; T, \mathbf{c})$
- 7: $\hat{\mathbf{z}} \leftarrow \frac{1}{\sqrt{\bar{\alpha}_T}}(\mathbf{z}_T - \sqrt{1 - \bar{\alpha}_T}\hat{\mathbf{v}}_0)$
- 8: $\hat{\mathbf{x}} \leftarrow D_{\theta}(\hat{\mathbf{z}})$
- 9: $\mathcal{L}_{\text{data}}(\hat{\mathbf{x}}, \mathbf{x}) \leftarrow \mathcal{L}_{\text{MSE}}(\hat{\mathbf{x}}, \mathbf{x}) + \lambda_{\text{LPIPS}}\mathcal{L}_{\text{LPIPS}}(\hat{\mathbf{x}}, \mathbf{x})$

- 10: $\mathbf{m} \leftarrow \mathcal{F}^{-1}[\mathbf{h} \cdot \mathcal{F}[\hat{\mathbf{z}}]]$ \triangleright Latent space HF mask
- 11: $\epsilon \sim \mathcal{N}(0, \mathbf{I})$
- 12: $t \sim [20, 980]$
- 13: $\hat{\mathbf{z}}_t \leftarrow \alpha_t \hat{\mathbf{z}} + \beta_t \epsilon$
- 14: $\mathbf{v}_{\phi} \leftarrow \Omega_{\phi}(\hat{\mathbf{z}}_t; t, \mathbf{c})$
- 15: $\mathbf{v}_{\phi'} \leftarrow \Omega_{\phi'}(\hat{\mathbf{z}}_t; t, \mathbf{c})$
- 16: $\omega \leftarrow \frac{1}{\text{mean}(\|\hat{\mathbf{z}} - \mathbf{v}_{\phi}\|^2)}$
- 17: $\mathcal{L}_{\text{VSD-HF}}(\hat{\mathbf{x}}) = \mathcal{L}_{\text{MSE}}(\hat{\mathbf{z}}_t, \hat{\mathbf{z}}_t - \mathbf{m} \odot \omega(\mathbf{v}_{\phi'} - \mathbf{v}_{\phi}))$

- 18: $\epsilon \sim \mathcal{N}(0, \mathbf{I})$
- 19: $t \sim [0, 1000]$
- 20: $\hat{\mathbf{z}}_t \leftarrow \alpha_t \hat{\mathbf{z}} + \beta_t \epsilon$
- 21: $\mathcal{L}_{\text{diff}} \leftarrow \mathcal{L}_{\text{MSE}}(\Omega_{\phi}(\hat{\mathbf{z}}_t; t, \mathbf{c}), \epsilon)$

- 22: Update θ using $\mathcal{L}_{\text{data}} + \lambda\mathcal{L}_{\text{VSD-HF}}$
- 23: Update ϕ using $\mathcal{L}_{\text{diff}}$
- 24: **end for**
- 25: **end procedure**

Algorithm 2 Inference Procedure

Load trained Ω_{θ} , E_{θ} , D_{θ} , Y

- 1: **procedure** INFER(Dataset $\mathcal{D}_{\text{test}}$)
- 2: $\mathbf{y} \sim \mathcal{D}_{\text{test}}$
- 3: $c \leftarrow Y(\mathbf{y})$
- 4: $\mathbf{z}_T \leftarrow E_{\theta}(\mathbf{y})$
- 5: $\hat{\mathbf{v}}_0 \leftarrow \Omega_{\theta}(\mathbf{z}_T; T, \mathbf{c})$
- 6: $\hat{\mathbf{z}} \leftarrow \frac{1}{\sqrt{\bar{\alpha}_T}}(\mathbf{z}_T - \sqrt{1 - \bar{\alpha}_T}\hat{\mathbf{v}}_0)$
- 7: $\hat{\mathbf{x}} \leftarrow D_{\theta}(\hat{\mathbf{z}})$
- 8: **return** $\hat{\mathbf{x}}$
- 9: **end procedure**

D.3. Super resolution agnostism

During the inference, we can use different upsampling scales since the model is trained to improve particular high frequencies. Thus, we show some zero-shot results from

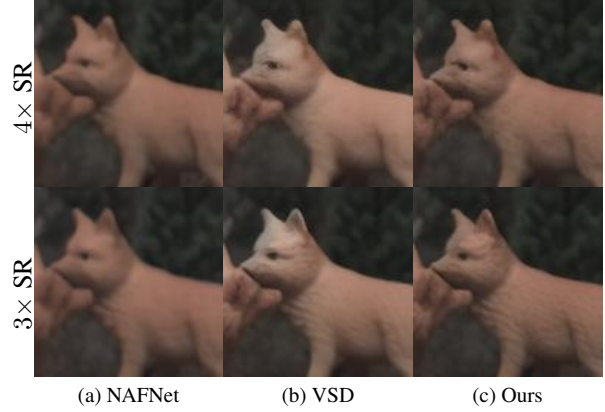


Figure 13. Qualitative comparison of our method with adversarially-trained baseline (NAFNet) and generative baseline (OSDiff) for 4 \times and 3 \times super-resolution (SR). Our model demonstrates better feature reconstruction under different SR factors.

3 \times and 8 \times super-resolution using the same model, which is trained to predict the 4 \times super-resolution. The qualitative results in Fig. 16 demonstrate that our method achieves comparable performance across various super-resolution scales.

D.4. Other techniques for alignment

We trained the Variational Auto Encoder (VAE) separately to verify the quality of encoding using different alignment approaches. First, we used deformable convolution layers [5] in intermediate steps of the encoder. However, this method is difficult to implement on hardware. We also tried to align RAW frames using Fourier Neural Operators (FNO) [17], where its Fourier Layer performs a global convolution using the Fourier transform. We used multiple stacked FNO layers in the encoder for frame alignment. However, the STNs performed better and had less complexity when aligning frames, and thus, we used STNs as the alignment operator in the encoder. The VAE reconstruction performance of the STNs, Deformable convolution layers, and FNOs is illustrated in Fig. 17 where these VAEs are trained independently after initializing the weights using a pretrained Stable Diffusion 2.1 [26] VAE.

E. User study

For the user study, we used images from NAFNet (yielding the best quantitative results from adversarially trained methods), OSDiff (utilizing VSD loss for image super-resolution), and our own method. We employed a two-level randomization design to ensure the study’s validity. First, the presentation order of the 30 randomly selected crops was randomized for each subject. This standard procedure

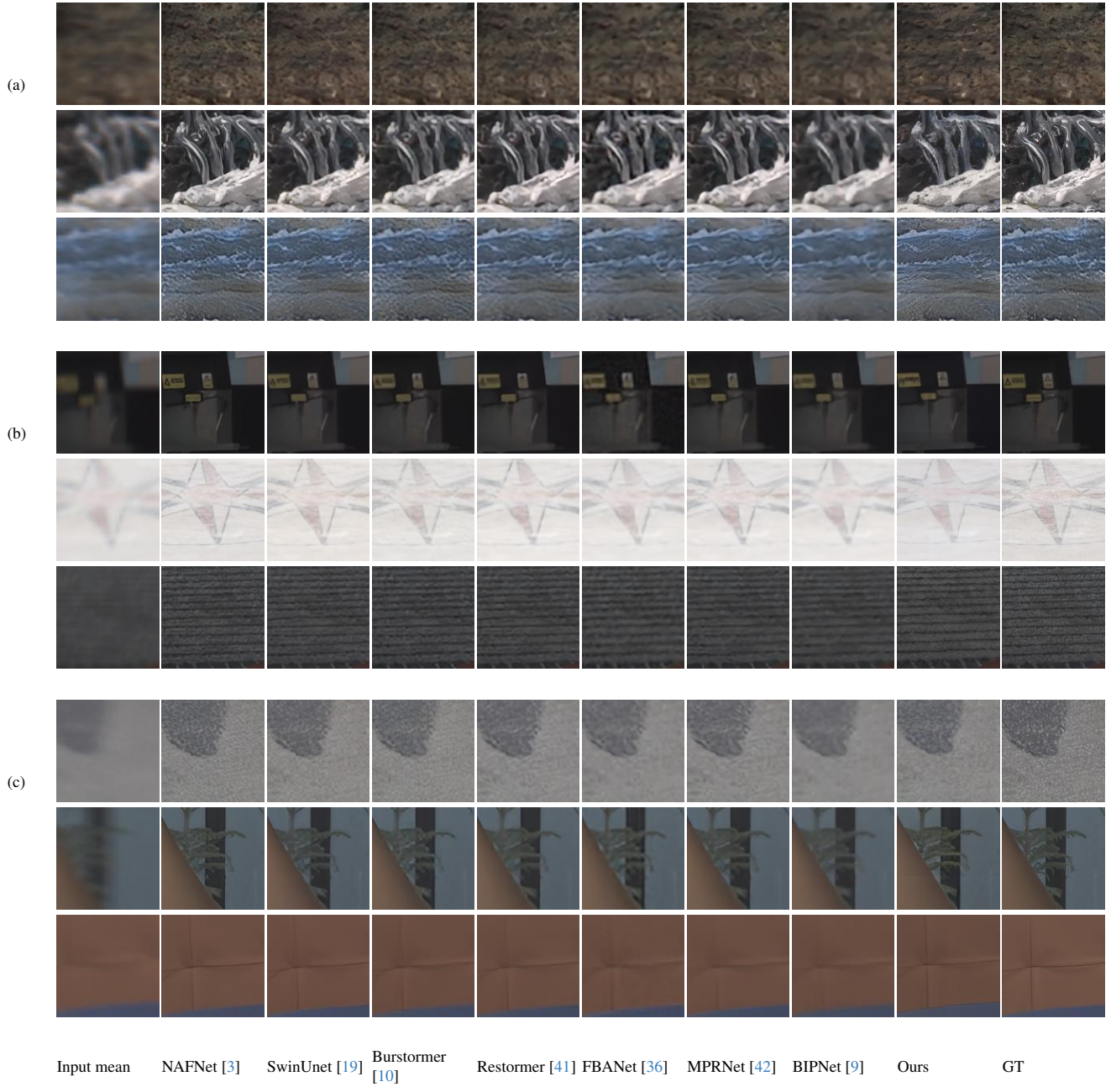
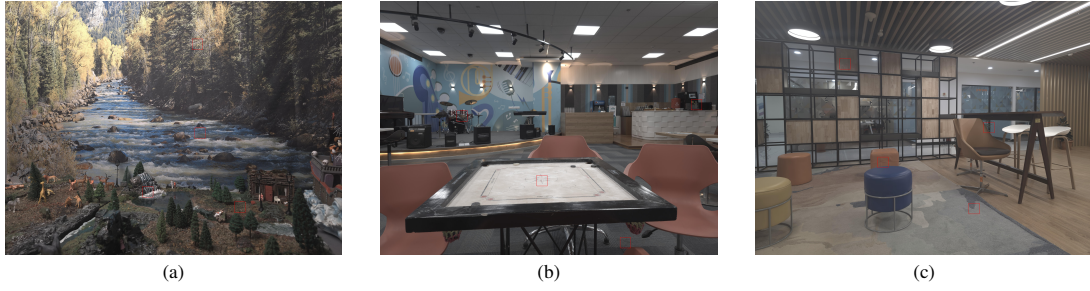


Figure 14. Qualitative comparison of different adversarial learning based postprocessing algorithms for generating RGB images using multi-frame RAW frames as input. Best viewed zoomed in.

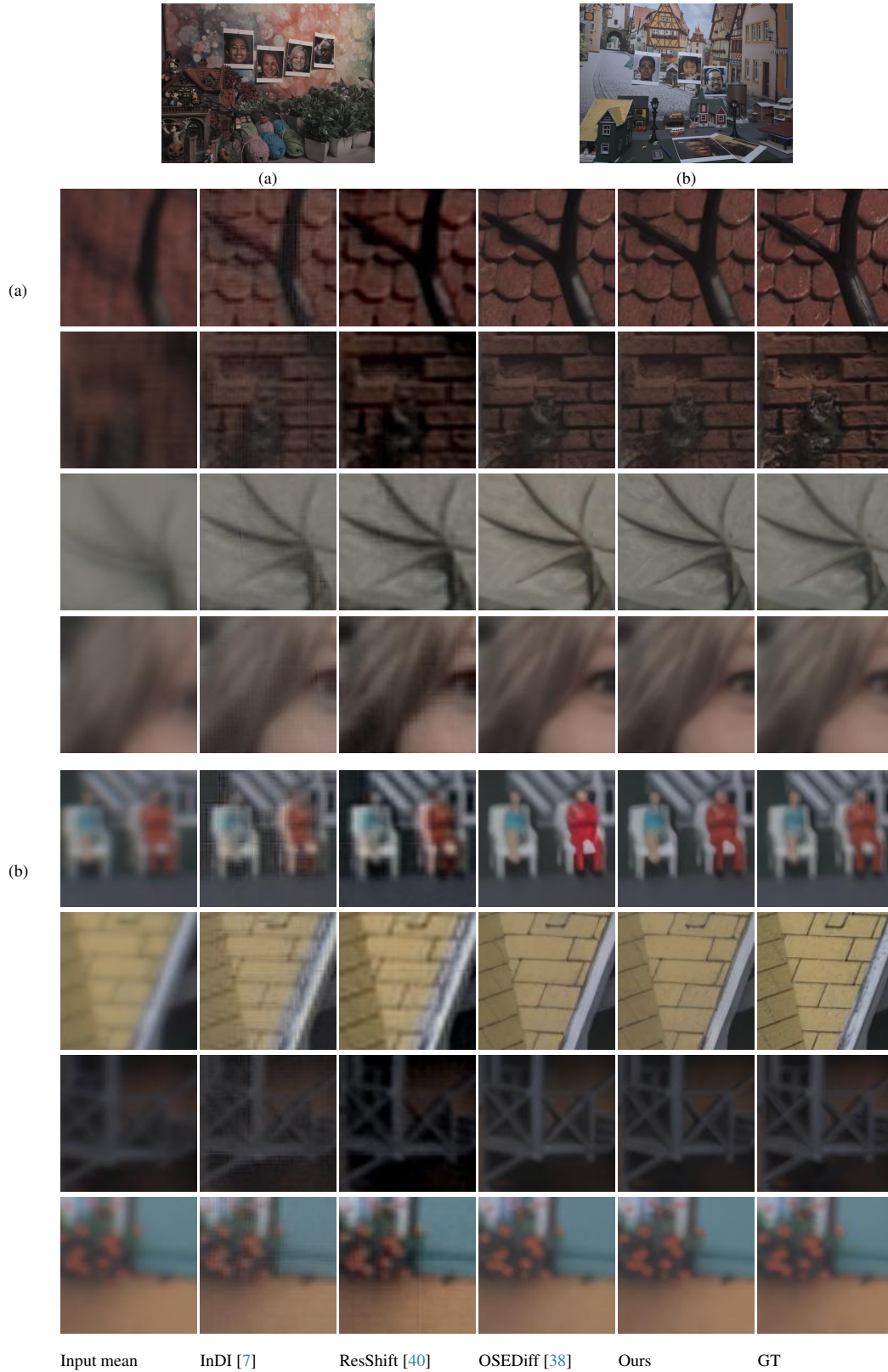


Figure 15. Qualitative comparison of different diffusion-based postprocessing algorithms for generating RGB images using multi-frame RAW frames as input. Best viewed zoomed in.

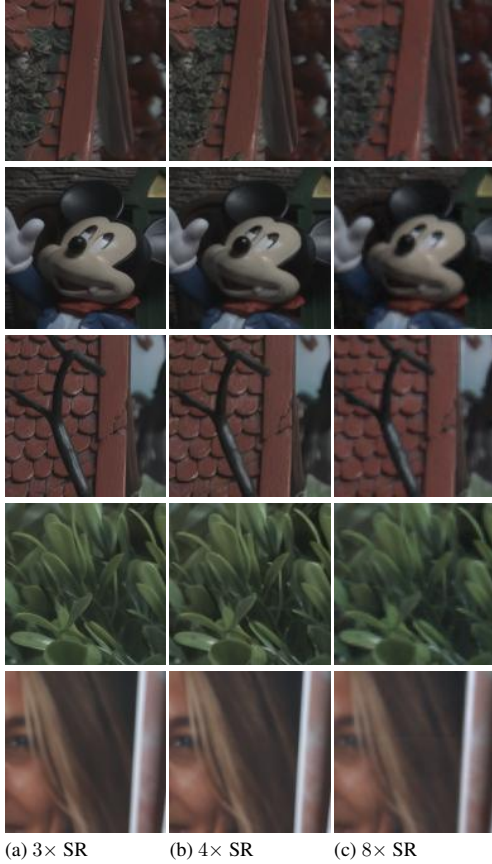


Figure 16. Qualitative results of our method on 3×, 4×, and 8× super resolution.



Figure 17. Performance of different alignment techniques used for RAW multi-frame alignment. STNs demonstrate slightly better visual quality when compared to other methods.

mitigates rater fatigue, a known decline in evaluator precision and consistency over time, and prevents sequential bias, which could unfairly penalize a method consistently shown at the end of the study. Second, within each trial, the spatial order of the three outputs (NAFNet, VSD, and GenMFSR) was also randomized. This prevents positional bias, where a rater might develop a preference for a specific on-screen location (e.g., left, middle, or right) or memorize a pattern. The images used in this study are shown in Fig. 18.

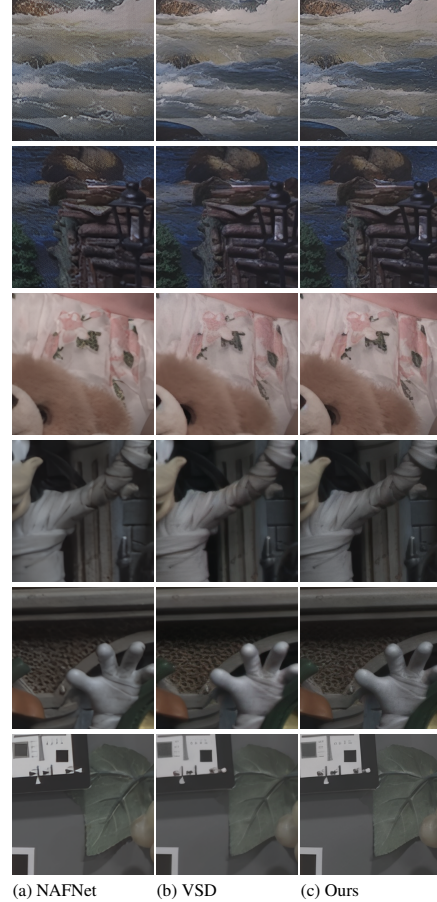


Figure 18. Samples of the figures used in the user study

F. Q&A

1. **Clarification on the contributions.** The core contribution of this paper is the system-level implementation of the burst RAW-to-RGB problem. We utilize STNs for alignment and propose a new loss for high-frequency detail generation. We moved the VSD loss descriptions to the supplement. to avoid distracting the reader.
2. **Further details about baseline architecture modifications to accommodate multi-frame inputs.** Changes to baselines are described in the experiments section.
3. **There is no comparison with the RGB-to-RGB performance of these methods.** Raw-to-RGB vs RGB-to-RGB is an irrelevant question. Once the image is converted to the RGB domain, some information is already lost at the ISP stage, defeating the whole purpose of improving RAW-to-RGB conversion.
4. **There are not enough details about the dataset.** Dataset collection details are available in the methodology section.
5. **While the paper highlights the use of “single-step diffusion” to enhance computational efficiency, it does**

not present concrete metrics such as inference-time latency, FLOPs, or memory usage. Refer to Tab. 2 in the main manuscript.

6. **There is a substantial gap in fidelity metrics compared to regression-based methods.** The authors agree with the accusation. However, the purpose of the generative model is to generate sub-pixel information, which reduces the performance on fidelity metrics as shown in the literature. We show better qualitative results to counter this argument and also with better perception quality metrics further reinforce this claim.
7. **The visual evidence provided in the ablation studies is unconvincing.** We have highlighted the visual results and quantitative results in the ablation study section.
8. **The presentation quality and diagram clarity require improvement.** Improved aesthetic polish of the figures.